Stereoscopic high-speed imaging for 3D tracking of coughed saliva droplets in the context of COVID-19 spreading

Roth, Adrian; Mehdi, Stiti; Frantz, David; Berrocal, Edouard

Published in:
Proceedings of the 20th International Symposium on Application of Laser and Imaging Techniques to Fluid Mechanics 2022

2022

Stereoscopic high-speed imaging for 3D tracking of coughed saliva droplets in the context of COVID-19 spreading

Adrian Roth[1,*], Mehdi Stiti[1], David Frantz[1] and Edouard Berrocal[1]

1: Division of Combustion Physics, Department of Physics, Lund University, Sweden
*Corresponding author: adrian.roth@forbrf.lth.se

Keywords: Particle Tracking Velocimetry, 3D, high-speed, droplets, COVID19.

ABSTRACT

Droplets generated by talking and coughing play a major role in the spreading of COVID-19. There is thus a need for accurate measurements of the physical properties of exhaled droplets, including their number, speed and direction. Several challenges are associated with imaging coughed droplets such as high droplet speed near the mouth where both short exposure time to freeze droplet motion and kHz recording rate to resolve their displacement is required. In addition, as a highly non-symmetrical spray system is formed from a cough, three-dimensional visualization is necessary to faithfully capture coughing events. In this work, a 3D, high-speed imaging technique is presented that facilitates such challenging measurements. A laser beam with a probe volume 15 mm thick - 120 mm high is formed and illuminates droplets exiting the mouth imaged using two high-speed cameras. Data has been recorded for four different male subjects where 3D droplet speed and direction has been extracted for 10 coughs each. The maximum speed for a single cough has been estimated to vary between 11 and 45 m/s and the average droplet speed has been found to be in the range 6.5 - 8.7 m/s. These results will be used as input parameters to improve simulation models of droplet transport in the context of virus spreading.

1. Introduction

The COVID-19 pandemic has caused large disruptions in countries all over the world where the virus is accountable for millions of deaths. There is an understanding that the virus mainly spreads through droplets exhaled from people when speaking and coughing (World Health Organization, n.d.; Bourouiba, 2020; Zhang et al., 2020). This airborne spreading is an important factor connected to used mitigation regulations such as keeping distance and avoiding indoor crowding. To make educated decisions regarding these regulations both experimental and simulation research on aerosols produced from people speaking and coughing is needed. Especially information of the pathogen bearing droplets are of interest which, among other, includes their number, speed, and direction. In addition, since coughing is one of the more common symptoms and transmission vector of the COVID19 it is of interest to experimentally analyze coughing events and the aerosols produced by it.

There have been multiple experimental works dedicated to understanding features of the cough, as shown by reviews from Mahjoub Mohammed Merghani et al. (2021) and El Hassan et al. (2021). First, Bourouiba et al. (2014) has used high speed imaging to look at the droplet entrainment coefficients that is connected to how the coughed air is spreading during jet and puff stages. Here, the coughed air is first in a jet stage that is followed by a puff like cloud when the jet is dissolved. Then, there are examples using Particle Image Velocimetry (PIV) (Chao et al., 2009; Dudalski et al., 2020; Kwon et al., 2012; Savory et al., 2014; VanSciver et al., 2011; Zhu et al., 2006) where the subjects are coughing into air seeded with particles. The particles are illuminated by a laser and the scattered light is then imaged. With two or more images at different times, velocity vectors of the air can be extracted and analyzed. Another used technique is Schlieren photography (Tang et al., 2009, 2012) where indirectly the temperature gradients of the air is imaged. These temperature gradients are connected to gradients of refractive index that will refract light depending on the temperature. In the Schlieren optical system, the light that has not been refracted is rejected so that only the refracted light is imaged. This means that the warmer exhaled air from e.g. coughing is visible. Gupta et al. (2009) analyzed the coughing airflow through a spirometer that measures the air volume per unit time. Together with an estimated mouth opening area of a subject coughing, an initial speed value of the air at the mouth can be estimated. In addition, Gupta et al. performed imaging of a subject coughing out smoke which is similar to research by Nishimura et al. (2013). Listed below are speeds of coughing subjects that have been found in the mentioned literature.

- Chao et al. (2009) maximum air speed 10.2 m/s and 13.2 m/s for females and males respectively and an average initial air speed of 10.2 m/s.
- Kwon et al. (2012) average initial speed 10.6 m/s and 15.3 m/s for females and males respectively.
- VanSciver et al. (2011) average maximum speed 10.2 ± 6.7 m/s with a maximum speed range between 1.15 and 28.8 m/s.
- Zhu et al. (2006) initial speed 11.2 m/s.
- Tang et al. (2009) propagation speed 5 m/s and (Tang et al., 2012) propagation speed 2.2-5 m/s and 3.2-14 m/s for females and males respectively.
- Gupta et al. (2009) cough peak flow rate 1.6-6 l/s and 3-8.5 l/s for females and males respectively and mouth opening area 3.37 ± 1.4 cm^2 and 4.00 ± 0.95 cm^2 for females and males respectively. This corresponds to initial speeds between 4.7-17.8 m/s and 7.5-21.25 m/s.
- Nishimura et al. (2013) initial speed greater than 6 m/s.

Note here that there is a difference between the initial speed and the maximum speed. The initial speed is the speed of the air when exiting the mouth and the maximum speed has been observed at a short distance outside the mouth. This can be explained by how the cough jet flow initially

decreases in area even after exiting the mouth thus increasing air speed, a phenomenon known as the vena contracta effect (VanSciver et al., 2011). These speeds gives a range between 2.2 and 21 m/s. Here both different techniques and ways of measuring speeds within techniques are mixed which mean that the results are not directly comparable even though they are important for comparison with speeds produced estimated in this work. Another thing to note about the speed results in the list above is that results from Dudalski et al. (2020), Savory et al. (2014) and Bourouiba et al. (2014) have not been added to the list. The reason for this is that Dudalski et al. and Savory et al. have estimated speeds at a rather large distance from the coughing subjects mouth and are harder to compare with the others and the speeds found in this work. In addition, Bourouiba et al. is also excluded since it included no explicit speed results.

All of the mentioned techniques except (Bourouiba et al., 2014) have performed experiments that measure speeds of coughed air, and not the speed of droplets that are the actual spreaders of the virions. In addition, they are all either 2D or point-wise measurements. Since the cough is a 3D phenomenon where droplets are spreading the virions, 3D measurements of droplets are required to give the best understand of the spreading of the virions. To better understand droplets produced by coughs, we have devised an experiment using Continuous Wave (CW) lasers and high speed cameras to extract droplet 3D trajectories. From these tracks, information of droplet speeds, spread angles and retardation can be analyzed and the droplet velocities are resolved both spatially and in time. We have tracked droplets for four different male adults that have coughed 10 times each. The next section explains the used experimental setup in detail, followed by the post processing scheme used to go from recorded raw images to droplet 3D tracks. Then the results are shown and discussed followed by the conclusions of this work.

2. Experimental setup

The experimental setup used in this work is illustrated in Figure 1(a) and (b). Here, two CW lasers, at 4W 450 nm and 5W 512 nm respectively, are combined using a dichroic mirror to produce a beam with 120 mm height and 15mm thickness. Above this laser a subject is located that coughs downward. The droplets produced by the subject coughing that travel inside the laser beam scatter the light into two Phantom VEO 710L high-speed cameras (LaVision Research) in a stereo configuration. The cameras are recording with 15 000 frames per second and exposure time of 50 μs. Each recording of a cough consisted of almost 31 000 frames over a duration of $\sim$2 seconds and each frame had a resolution of 800x512 pixels, where each pixel had a size of around 200 μm. In Figure 1(C1) and (C2), example raw images from a recording of a cough is shown. Note here that the use of two lasers and the choice of setting the cameras at an angle of 54° to the laser direction enables the detection of smaller droplets. Unpublished results have found that this setup can detect droplets down to 10 μm if the droplet is located at the center of the laser beam.

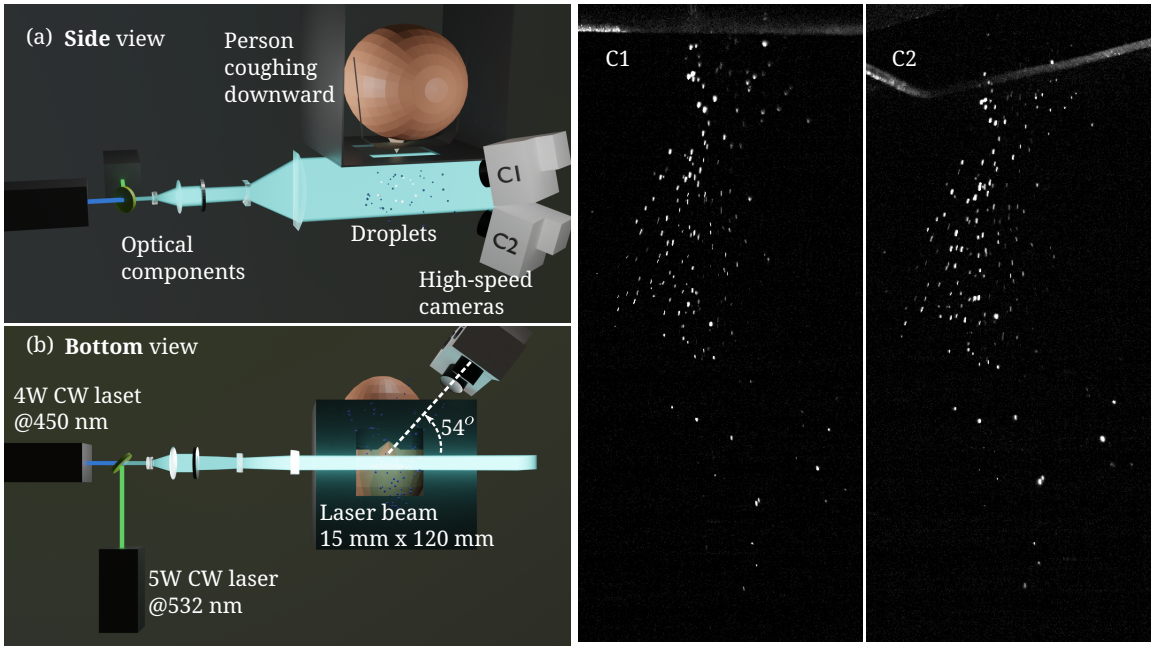

Figure 1. Illustration of the experimental setup and example raw data. (a) and (b) Experimental setup shown from the front and bottom respectively. Two CW lasers are combined to a single beam that is 120 mm high and 15 mm thick. A subject is coughing downward towards the beam and droplets traveling inside the beam scatter light into two high-speed cameras C1 and C2 recording at 15 kHz frame rate. On the right, raw data from the respective cameras recorded at the same time point is shown.

3. Extraction of droplet 3D trajectories

The velocity of coughed droplets is obtained through a post-processing scheme divided into three steps.

1. Finding the droplet coordinates in the images of each camera, Figure 2(a).
2. Triangulate the droplet positions in 3D with a camera calibration, Figure 2(b).
3. Use 3D Particle Tracking Velocimetry (3D-PTV) to extract droplet tracks together with droplet velocities, Figure 3 and 4.

The first step is to estimate the droplet coordinates in the images. From the raw images, pixels that include corrupting reflection of laser light are masked and a global intensity threshold is applied to detect and isolate the imaged droplets. All pixels with a value above 40 counts in the 12-bit images are defined as droplets. After the threshold, the found image areas of neighboring pixels are defined as droplet pixels. To get the droplet coordinates in the images, the weighted average of the pixel intensities and pixel coordinates in the collected areas are used. Having obtained droplet image coordinates from the cameras, it is possible to perform the second step and triangulate the 3D position of each particle. In order to achieve this, a camera calibration is required.

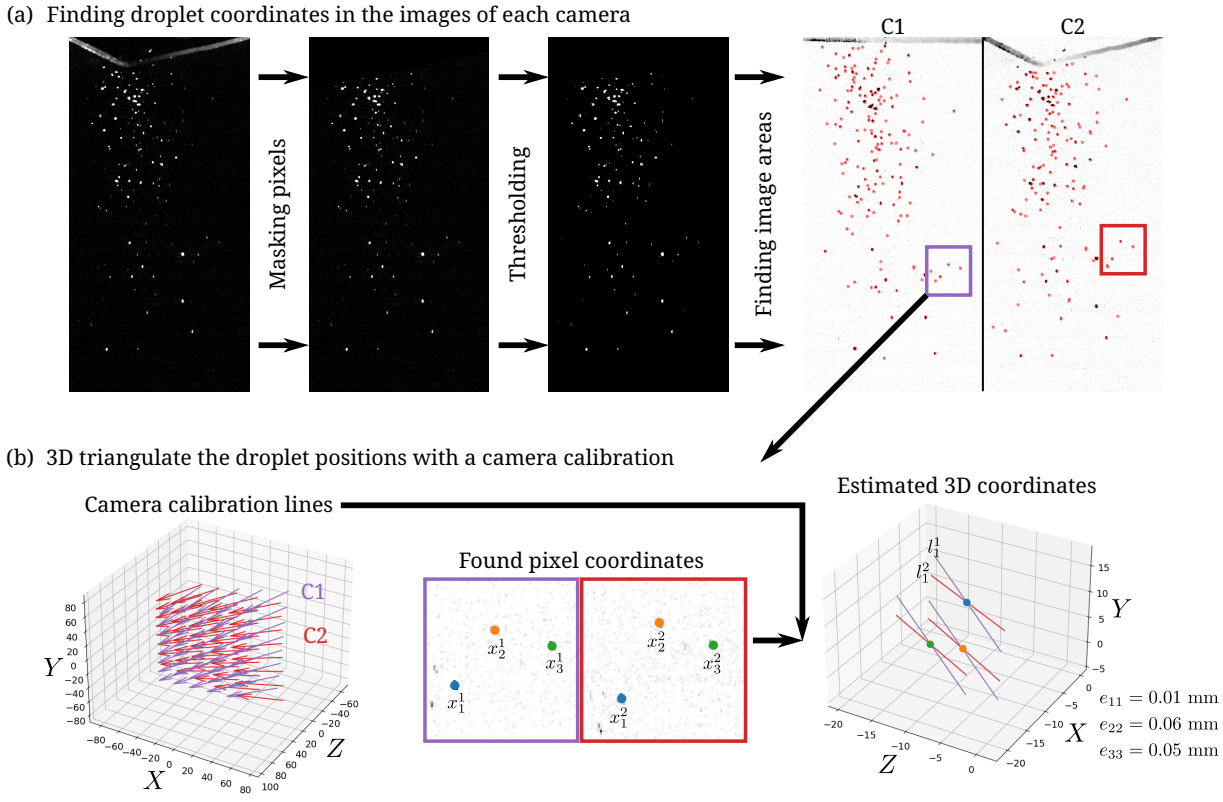

Figure 2. Illustration of the post processing procedure. (a) First the droplet coordinates in the images are found. (b) Then a camera calibration is used to match the particles between the cameras and find 3D coordinates.

In this work, the calibration scheme explained in Machicoane et al. (2019) is used. This scheme, in contrast to the common pinhole camera matrix approach (Tsai, 1987), estimates a correspondence between each pixel and a 3D line where a droplet found on this line will be imaged at the pixel location on the sensor. To estimate these 3D lines, a known pattern (here a checkerboard pattern with 19x10 intersections) is put on a rail. The world coordinate system is defined so that only the third dimension Z is changed while the X and Y are kept constant for the pattern moving on the rail. Then, images are recorded while moving the pattern to known locations on the rail. We used 16 different steps from $Z = 0$ to $Z = 15$ mm. Since the pattern is known, we can for each location find multiple (in our case 190) point correspondences between camera coordinates and world coordinates for the pattern. With these correspondences, coefficients for a 2D polynomial transform are estimated that goes from the camera (x, y) coordinates to the world (X, Y). With a transform polynomial $\mathcal{L}$ of order 2 or higher, imaging distortions are taken into account. We used order 3 polynomials as suggested by Machicoane et al. that have 10 coefficients for X and Y respectively as seen in the following equation:

$$\mathcal{L}(x,y) = \begin{pmatrix} a_0^X + a_1^X x + a_2^X y + a_3^X x^2 + a_4^X y^2 + a_5^X xy + a_6^X x^3 + a_7^X y^3 + a_8^X x^2 y + a_9^X xy^2, \\ a_0^Y + a_1^Y x + a_2^Y y + a_3^Y x^2 + a_4^Y y^2 + a_5^Y xy + a_6^Y x^3 + a_7^Y y^3 + a_8^Y x^2 y + a_9^Y xy^2 \end{pmatrix}. \quad (1)$$

This transformation is used to get world (X, Y) coordinates for each pixel and each Z location on

the rail. This means that each pixel has multiple 3D world points (in our case 16) that are all imaged by this pixel. Finally, the 3D line for each pixel is estimated by a total least square algorithm. While this scheme requires the use of a rail or some other way to know the coordinates and orientation of all patterns, it is very versatile when it comes to taking imaging distortions into account and can in addition easily be used in camera calibration of systems with complex refraction properties.

The next processing step is to use this calibration to estimate droplet 3D coordinates by finding which of the found droplets in each camera correspond to the same one in 3D space. Here, the pixel coordinates from both cameras are denoted x_i^c for camera c and point number i at one recorded time point for the cameras. From the calibration each of these coordinates is connected to a line l_i^c. Here, non-integer coordinates are linearly interpolated from the 3D lines of surrounding pixels. Each line is defined by a 3D point $\mathbf{q}_i^c$ and a direction $\mathbf{v}_i^c$ where all points $\mathbf{p}_i^c$ on the line can be reached through:

$$l_i^c = \{\mathbf{p}_i^c \mid \mathbf{p}_i^c = \mathbf{q}_i^c + \lambda_i^c \mathbf{v}_i^c, \lambda_i^c \in \mathbb{R}\}. \tag{2}$$

To find a droplet position, the corresponding line for the droplet coordinates in each of the cameras, l_i^1, l_j^2, are used. There is a point on each line where the lines are closest to one another. To find the $\lambda_i^{1,\text{closest}}$ and $\lambda_j^{1,\text{closest}}$ corresponding to these points the following calculation is performed:

$$\begin{bmatrix} \lambda_i^{1,\text{closest}} \\ \lambda_j^{2,\text{closest}} \end{bmatrix} = \begin{bmatrix} ||\mathbf{v}_i^1||^2 & -\mathbf{v}_i^1 \cdot \mathbf{v}_j^2 \\ -\mathbf{v}_j^2 \cdot \mathbf{v}_i^1 & ||\mathbf{v}_j^2||^2 \end{bmatrix}^{-1} \begin{bmatrix} \mathbf{v}_i^1 \cdot (\mathbf{q}_j^2 - \mathbf{q}_i^1) \\ \mathbf{v}_j^2 \cdot (\mathbf{q}_i^1 - \mathbf{q}_j^2) \end{bmatrix}. \tag{3}$$

Here $\mathbf{u} \cdot \mathbf{v}$ is the scalar product between vectors. With the estimated λ the points are estimated as:

$$\begin{aligned} \mathbf{p}_j^{1,\text{closest}} &= \mathbf{q}_i^1 + \lambda_j^{1,\text{closest}} \mathbf{v}_i^1 \\ \mathbf{p}_j^{2,\text{closest}} &= \mathbf{q}_i^2 + \lambda_j^{2,\text{closest}} \mathbf{v}_i^2 \end{aligned} \tag{4}$$

The length of the line between these points $||\mathbf{p}_j^{2,\text{closest}} - \mathbf{p}_i^{1,\text{closest}}||$ is defined as the matching error e_{ij}. Trying all the possible combinations of found drops in each camera gives a matching error matrix with the number of rows equal to the number of found droplets in the first camera and number of columns is the corresponding number for the second camera. To, at each time point, draw the first possible match, the minimum value of this matrix is extracted, (i', j'). If this error $e_{i'j'}$ is smaller than a max matching error threshold (here set to 0.2 mm) the match is valid, and a 3D point is calculated as the center of the line used before to define the matching error. Finally, the two points in each of the cameras are marked as used. The process of finding minimum matching error and attempting matching is repeated until the matching error exceeds the threshold for this time point. Then the same process is used for each time point in the recording.

With known 3D coordinates of droplets, it is possible to extract velocities by tracking the droplets. Here a track is estimated as a sequence of droplet 3D positions over different frames. The 3D-PTV tracking algorithm used here is inspired by the Four Frame Best Estimate (FFBE) method by Ouellette et al. (2006) and the extension by Clark et al. (2019). FFBE uses the estimated velocity and acceleration vector to try and extrapolate the droplet position in future frames. With two known

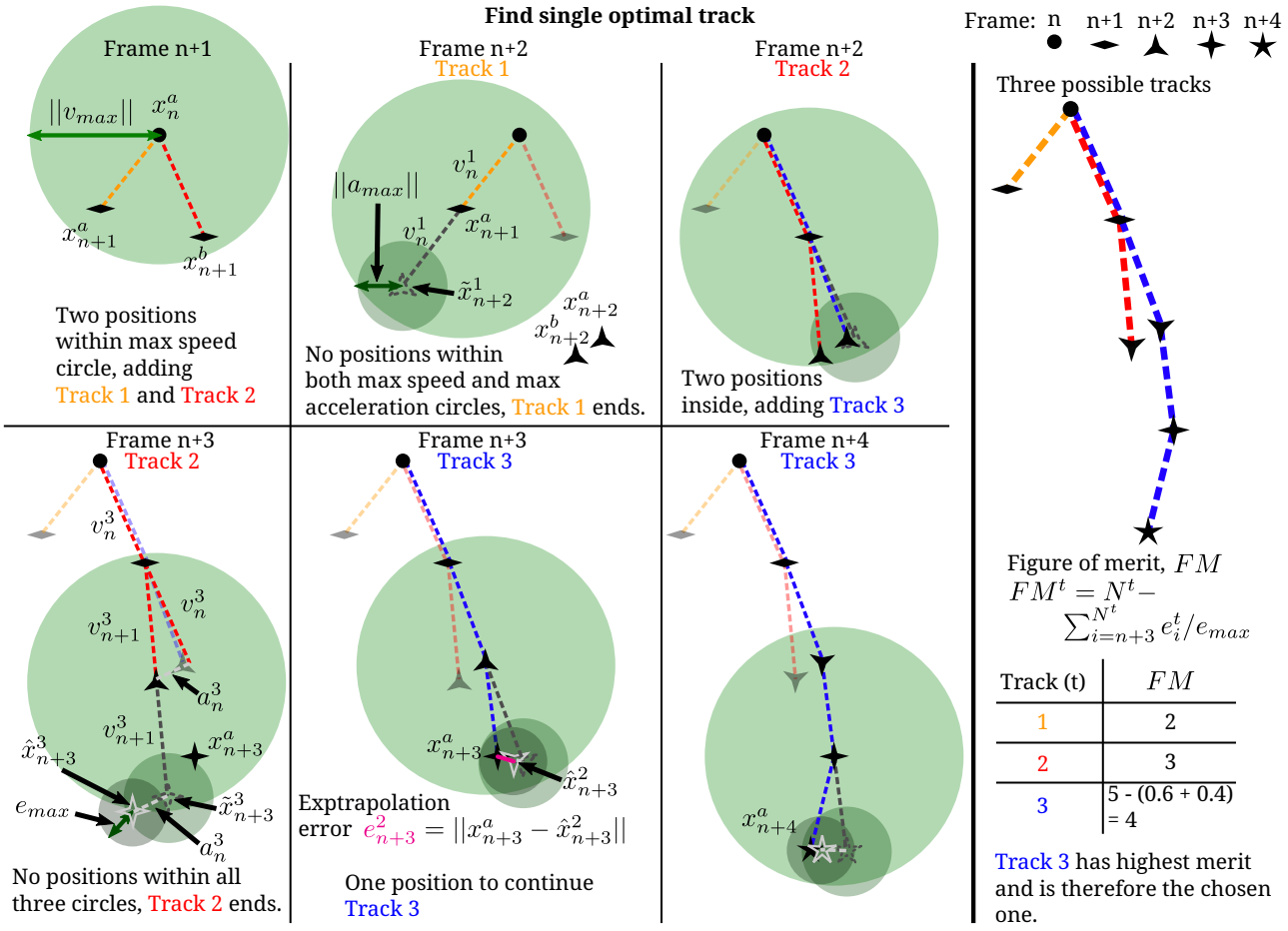

Figure 3. Illustration of the post processing tracking from a single starting position in 2D. This is a recursive technique that in the first step takes all droplet positions within a maximum speed $||v_{max}||$. For each of these the track is continued by extrapolating the track's next position using previous velocity. All positions inside a maximum absolute acceleration $||a_{max}||$ is here chosen recursively. Then, both previous velocity and acceleration is used in extrapolation. Here, droplet positions closer than the maximum extrapolation error e_{max} to the extrapolated position is added in the recursion. This is continued until no more positions are found. In the final tree, the Figure of Merit FM showed on the bottom right in the figure is used to find the optimal track from a single starting position.

positions (x_n and x_{n-1}, n is latest frame number) of a track, the current velocity of the track can be estimated as,

$$v_n = \frac{x_n - x_{n-1}}{\Delta t}, \tag{5}$$

where Δt is the time between frames, ~67 μs for our measurements. This can then be used to extrapolate the next position of the track,

$$\hat{x}_{n+1} = x_n + v_n \Delta t. \tag{6}$$

A track with at least three positions (x_n, x_{n-1} and x_{n-2}) has an estimated acceleration vector,

$$a_n = \frac{x_n - 2x_{n-1} + x_{n-2}}{\Delta t^2}, \tag{7}$$

The extrapolation position is then,

$$\hat{x}_{n+1} = x_n + v_n \Delta t + a_n \Delta t^2. \tag{8}$$

Then the distance from the extrapolated position to actual droplet positions in the next frame is calculated as the extrapolation error e,

$$e_{n+1} = ||x_{n+1} - \hat{x}_{n+1}|| \tag{9}$$

The found droplet with minimum extrapolation error is used as the most probable continuation of the track. However, at the initial phase of a track neither the velocity nor acceleration is known. Here, Clark et al., suggested to recursively try all different combinations of droplets in the following four frames within limiting ranges of maximum speed and maximum absolute acceleration. Compared to the first proposed FFBE using nearest neighbor, this approach increases accuracy in the tracking. We have further developed the recursion to not only include the first four frames, but instead all frames to the end of the track (Figure 3). A recursive tree is extracted with all possible continuations of the droplet track from a single start position and frame. The tree is limited by predefined maximum speed, maximum absolute acceleration and a maximum extrapolation error. The final track chosen for the starting position is the branch from root to leaf along the tree that has the largest Figure of Merit FM, defined as:

$$FM^t = N^t - \sum_{i=n+3}^{N^t} e_i^t / e_{max} \tag{10}$$

Here, t is the reference to a specific branch in the tree from the root to a leaf with specific length N^t, and extrapolation errors e_i^t for the frame i in the track. Note that only tracks longer than 3 will have any extrapolation errors and the error is scaled by the used maximum extrapolation error to get a comparable merit value with the track length for different tracking situations. In this work, a minimum track length of six frames is used to verify that a track is correct. Now a track has been found for a single starting droplet position, the next problem is to choose which are the best starting positions to avoid tracking conflicts.

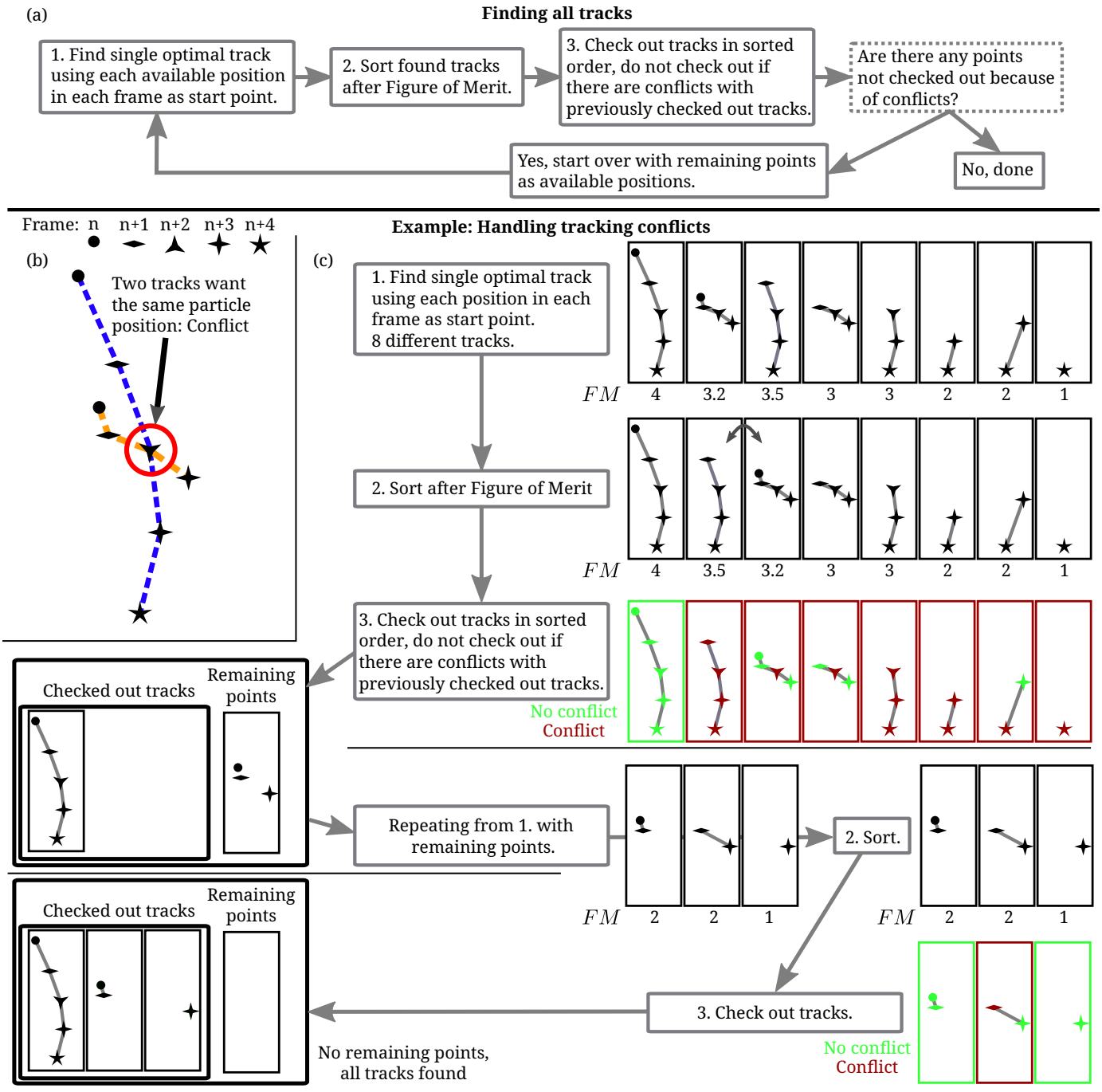

Figure 4. Illustration of the post processing to find all tracks. (a) Flowchart of how tracks are found and prioritized. (b) Example of a situation of tracking conflict in 2D. (c) Application of the procedure to find all tracks of the example in (b). Here, to find an optimal track from a single starting position use the procedure illustrated in Figure 3.

Now we have an algorithm to find a single track from a single starting point. The next question is how to organize the finding of all tracks, which starting points should the algorithm start with to find tracks. A simple solution is to start with the positions in the first frame and then move on. However, then the assumption is made that tracks starting earlier are more important and in the case of a conflict (Figure 4(b)), where two tracks want the same droplet position in a frame,

the track that started earliest will be favored. This is definitely not always the correct case and in addition the approach does not take into account conflict of tracks that starts in the same frame. Our approach is instead to let the mentioned Figure of Merit decide which tracks should be favored in conflicts. By following the flowchart in Figure 4(a), tracks starting at droplet positions that in the end gives a higher FM are preferred no matter at which frame the track starts. An example is shown in Figure 4(c) as to how this procedure works.

The search algorithm to find all tracks can be quite computationally intensive. To reduce this there is firstly the mentioned limitation in the search tree with maximum speed, maximum absolute acceleration and maximum extrapolation error when finding the track for a single starting point. In addition, a dynamic programming approach is used. When a single optimal track has been found after traversing its corresponding sub-tree the result is saved with reference to the first three droplet positions in this track. When a second track has the same three droplets as its last three, the optimal track from the saved sub-tree can be reused instead of traversing it again. This largely optimizes computations since there are a lot of tracks with the overlapping sub-trees in this algorithm.

4. Results and discussion, droplet speed and direction

With the droplet 3D tracks found, the difference between coordinates in two consecutive frames is used to estimate the instantaneous droplet velocity where its absolute value is the instantaneous droplet speed. The droplet speed is then defined as the average of all instantaneous speeds obtained along its track. Example results of trajectories from subject 1 and 6 different coughs are shown in Figure 5 where the origin of the cough is at the top of each 3D plot.

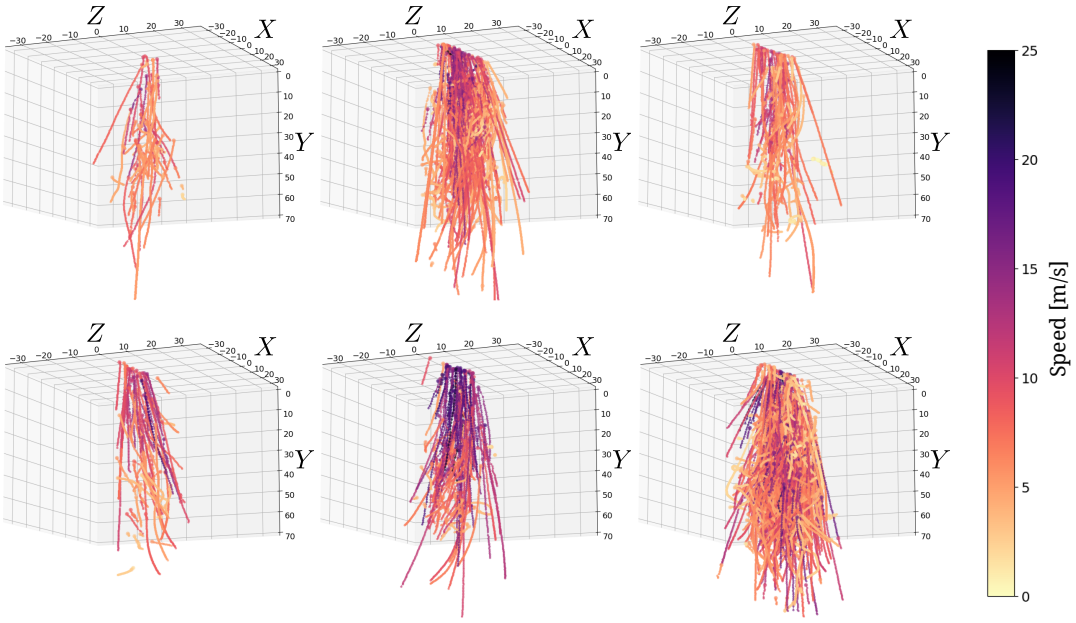

Figure 5. Example droplet 3D trajectories from 6 different cough events from subject 1. Here, the color shows the average speed of each droplet.

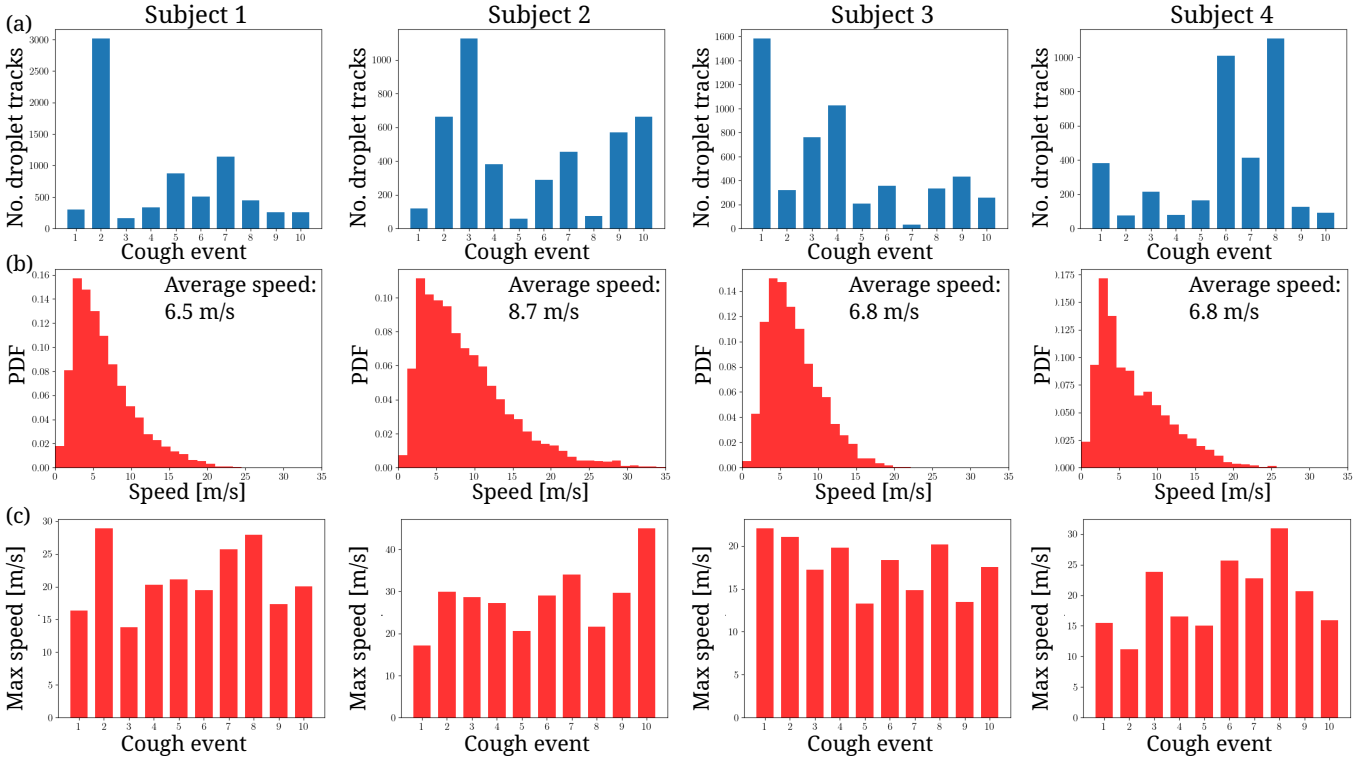

Figure 6. Accumulated droplet speed results for all four subjects. (a) The number of found tracks for each of the 10 cough events and subject. (b) A histogram of the droplet speed distribution accumulated for all 10 coughs. (c) The maximum droplet speed for each cough event. (d) Spatial velocity map showing the average of instantaneous speeds and direction at different positions in the 3D coordinate system accumulated for all 10 coughs.

Further analysis of the different subjects have been performed and are visualized in Figures 6 and 7. For each subject, 10 different coughs have been processed. Here, 6(a) shows the number of tracks found for each cough. Note that this does not correspond to the number of expelled droplets in a cough since not all droplets are entering the laser beam with the current experimental setup. In addition, since the coughing subject was left some freedom to cough naturally, the direction of the coughs differed where some of them aligned better with the laser beam. This together with the natural change of number of produced droplets from a cough explains the large variation in found droplets between coughs.

6(b) shows a histogram of the distribution of droplet speeds for all 10 coughs ranging between 0 and 35 m/s. The found average of this distribution for each subject is 6.5 $\pm$ 4.0 m/s, 8.7 $\pm$ 5.7 m/s, 6.8 $\pm$ 3.5 m/s and 6.8 $\pm$ 4.6 m/s. The average speed is around 6.7 m/s for three subjects and subject 2 has a higher average speed of 8.7 m/s. Here, it seems like the distribution mode (peak PDF) is approximately at the same speed for all subjects. This can be connected to a large number of slower droplets that are traveling out from the jet and slow down. Otherwise the speed distributions above the mode speed is varying between the subjects where e.g. subject 1 has a steeper slope, slower droplets, compared to subject 2.

6(c) Show the maximum droplet speeds for each cough event. This is an important cough feature since it is connected to the maximum distance the droplets can travel and also possibly spread virions. Generally speeds between 20 and 30 m/s are found where subject 3 has somewhat lower maximum speeds. Comparing this to the literature the speeds found in this work seems to be larger than what has been previously found. The reason for this is firstly that our results measure 3D speeds. The 3D speed will always be larger or equal to the corresponding 2D speeds. However, this is probably not the whole reason, instead these results suggest that droplet speeds measured in this work are larger than air flow speeds, measured in the literature.

Figure 7(d) show spatial velocity maps where the droplet instantaneous velocities have been used. For each cough the droplet trajectories have been normalized to have the same origin and general direction in the positive Y-direction (this can as mentioned differ between coughs). Three different plots have been produced for each subject. These are cross sections of the different combinations of dimension XY, XZ and YZ. For each of these combinations the coordinates are divided into small boxes and all instantaneous velocities found inside each box is averaged to get a speed and direction. Here, the arrows indicate the direction and the color the speed. The cough jet at the center of each subjects XY map that has a higher speed. Less clear is that the drops are spreading from a center of $X = Z = 0$ in XZ plot that is expected. In addition, one can notice the displacement of maximum speed in the Y dimension connected to the vena contracta effect (explained in the introduction). This is extra visible for subject 2 with maximum at 40 mm from the top of the laser beam. Since the subject is approximately 20 mm from the beam the maximum speed is 60 mm from the mouth.

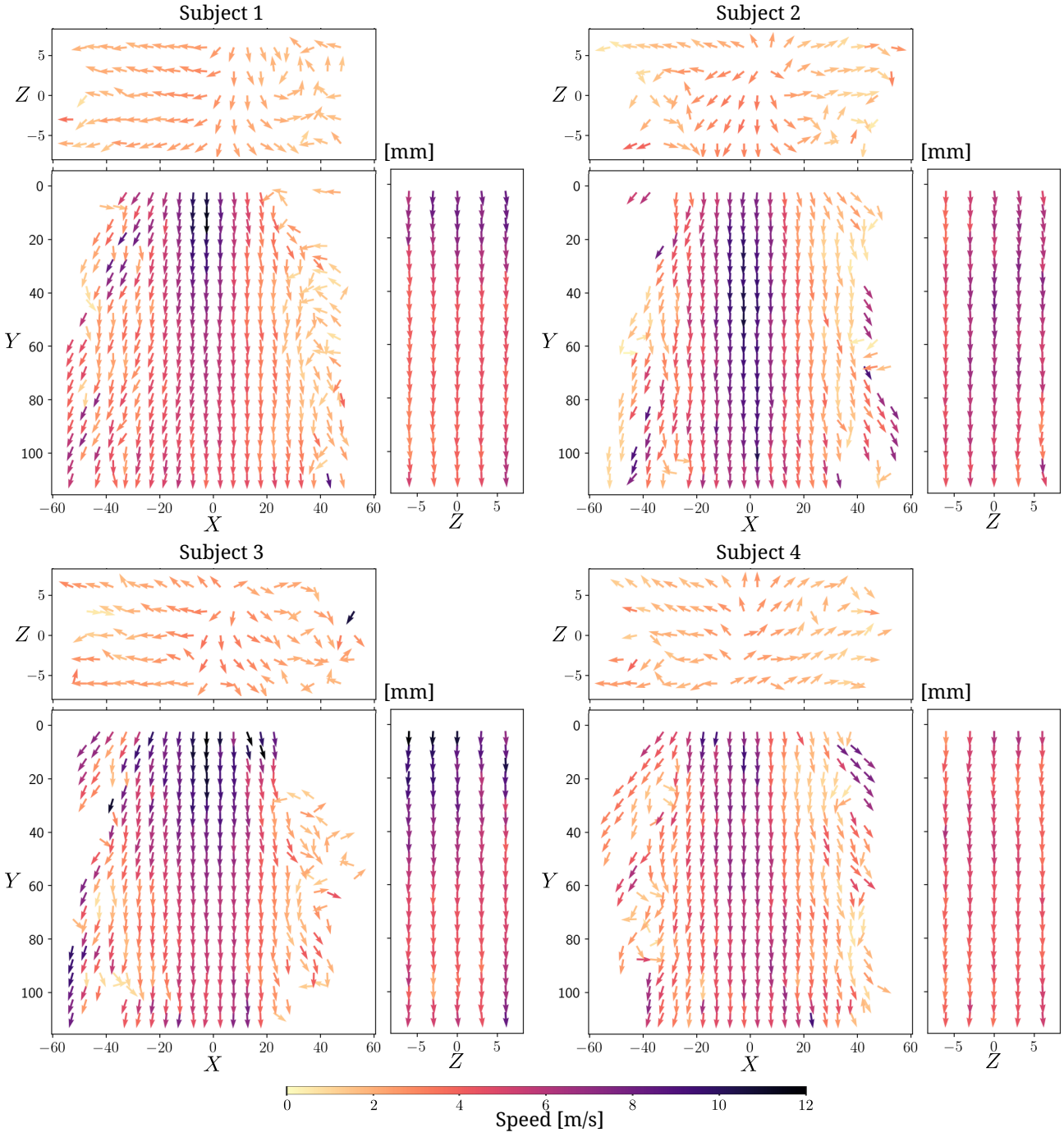

Figure 7. Spatial velocity quiver maps for all four subjects. Here the average of instantaneous speeds and direction at different positions in the 3D coordinate system accumulated for all 10 coughs are showed.

5. Conclusion

In this work coughed droplet 3D trajectories and velocities have been measured with an experimental setup using two CW lasers and a stereo high-speed camera configuration. Measurements for 4 different male subjects and 10 coughs each have been analyzed. Here, it has been found that the maximum droplet speeds are larger than the ones found in the literature. This can be explained by that previous work has measured air speeds and not the droplets speed. Our results then suggests that the droplet speed is larger than the air speed. When comparing different subjects subject 1, 3 and 4 have similar average speeds around 6.7 m/s. Then interestingly subject 2 has a higher speed at 8.7 m/s.

In the future, to make the found velocity information even more useful, uncertainties in the tracking should be quantified. Here, one can deduce the limitations connected to for example droplet concentration and droplet speed. In addition, a deeper analysis of this data can be performed to find for example the propagation speed of the first droplets in each cough. These results will be valuable for modelers simulating the transport of droplets in the context of virus spreading.

Acknowledgments

The authors would like to acknowledge our funding from the Crafoord Foundation (202110942) and the Swedish Research Council (2021-04542).

Nomenclature

x, y	Coordinates in a recorded image.
x	The combination of both image coordinates
X, Y, Z	Global world coordinates.
$\mathcal{L}$	Transform to go from image coordinates to world coordinates in the X, Y plane.
v	velocity vector
a	acceleration vector
e	extrapolation error, the distance between the extrapolated point of a track where both the previous velocity and acceleration is used.
$\|\|v_{max}\|\|$	maximum speed
$\|\|a_{max}\|\|$	maximum absolute acceleration
e_{max}	maximum extrapolation error
FM	Figure of Merit for a track, a higher value corresponds to a better track.
l	a 3D line with from a point $\mathbf{q}$ and direction $\mathbf{v}$ where all λ scalars multiplied with $\mathbf{v}$ plus $\mathbf{q}$ is on the line.

References

Bourouiba, L. (2020, March). Turbulent Gas Clouds and Respiratory Pathogen Emissions: Potential Implications for Reducing Transmission of COVID-19. *JAMA*, *323*(18), 1837-1838. Retrieved 2021-01-26, from https://doi.org/10.1001/jama.2020.4756 doi:

Bourouiba, L., Dehandschoewercker, E., & Bush, J. W. M. (2014, April). Violent expiratory events: on coughing and sneezing. *Journal of Fluid Mechanics*, *745*, 537–563. Retrieved 2021-12-28, from https://doi.org/10.1017/jfm.2014.88 doi:

Chao, C., Wan, M., Morawska, L., Johnson, G., Ristovski, Z., Hargreaves, M., ... Katoshevski, D. (2009, February). Characterization of expiration air jets and droplet size distributions immediately at the mouth opening. *Journal of Aerosol Science*, *40*(2), 122–133. Retrieved 2021-05-19, from https://doi.org/10.1016/j.jaerosci.2008.10.003 doi:

Clark, A., Machicoane, N., & Aliseda, A. (2019, April). A quantitative study of track initialization of the four-frame best estimate algorithm for three-dimensional Lagrangian particle tracking. *Measurement Science and Technology*, *30*(4), 045302. Retrieved 2021-01-08, from https://doi.org/10.1088/1361-6501/ab0786 doi:

Dudalski, N., Mohamed, A., Mubareka, S., Bi, R., Zhang, C., & Savory, E. (2020, September). Experimental investigation of far-field human cough airflows from healthy and influenza-infected subjects. *Indoor Air*, *30*(5), 966–977. Retrieved 2021-12-30, from https://doi.org/10.1111/ina.12680 doi:

El Hassan, M., Assoum, H., Bukharin, N., Al Otaibi, H., Mofijur, M., & Sakout, A. (2021, December). A review on the transmission of COVID-19 based on cough/sneeze/breath flows. *The European Physical Journal Plus*, *137*(1), 1. Retrieved 2021-12-28, from https://doi.org/10.1140/epjp/s13360-021-02162-9 doi:

Gupta, J. K., Lin, C.-H., & Chen, Q. (2009, December). Flow dynamics and characterization of a cough: Flow dynamics and characterization of a cough. *Indoor Air*, *19*(6), 517–525. Retrieved 2021-12-28, from https://doi.org/10.1111/j.1600-0668.2009.00619.x doi:

Kwon, S.-B., Park, J., Jang, J., Cho, Y., Park, D.-S., Kim, C., ... Jang, A. (2012, June). Study on the initial velocity distribution of exhaled air from coughing and speaking. *Chemosphere*, *87*(11), 1260–1264. Retrieved 2021-05-19, from https://doi.org/10.1016/j.chemosphere.2012.01.032 doi:

Machicoane, N., Aliseda, A., Volk, R., & Bourgoin, M. (2019, March). A simplified and versatile calibration method for multi-camera optical systems in 3D particle imaging. *Review of Scientific Instruments*, *90*(3), 035112. Retrieved 2021-01-08, from https://doi.org/10.1063/1.5080743 doi:

Mahjoub Mohammed Merghani, K., Sagot, B., Gehin, E., Da, G., & Motzkus, C. (2021, January). A review on the applied techniques of exhaled airflow and droplets characterization. *Indoor Air*, *31*(1), 7–25. Retrieved 2021-01-26, from https://doi.org/10.1111/ina.12770 doi:

Nishimura, H., Sakata, S., & Kaga, A. (2013, November). A New Methodology for Studying Dynamics of Aerosol Particles in Sneeze and Cough Using a Digital High-Vision, High-Speed Video System and Vector Analyses. *PLOS ONE*, *8*(11), e80244. Retrieved 2021-12-30, from https://doi.org/10.1371/journal.pone.0080244 doi:

Ouellette, N. T., Xu, H., & Bodenschatz, E. (2006, February). A quantitative study of three-dimensional Lagrangian particle tracking algorithms. *Experiments in Fluids*, *40*(2), 301–313. Retrieved 2021-01-08, from https://doi.org/10.1007/s00348-005-0068-7 doi:

Savory, E., Lin, W. E., Blackman, K., Roberto, M. C., Cuthbertson, L. R., Scott, J. A., & Mubareka, S. (2014, December). Western Cold and Flu (WeCoF) aerosol study – preliminary results. *BMC Research Notes*, *7*(1), 563. Retrieved 2021-12-28, from https://doi.org/10.1186/1756-0500-7-563 doi:

Tang, J. W., Liebner, T. J., Craven, B. A., & Settles, G. S. (2009, December). A schlieren optical study of the human cough with and without wearing masks for aerosol infection control. *Journal of The Royal Society Interface*, *6*(suppl_6), S727-S736. Retrieved 2021-12-28, from https://doi.org/10.1098/rsif.2009.0295.focus doi:

Tang, J. W., Nicolle, A., Pantelic, J., Koh, G. C., Wang, L. D., Amin, M., … Tham, K. W. (2012, April). Airflow Dynamics of Coughing in Healthy Human Volunteers by Shadowgraph Imaging: An Aid to Aerosol Infection Control. *PLoS ONE*, *7*(4), e34818. Retrieved 2021-12-28, from https://doi.org/10.1371/journal.pone.0034818 doi:

Tsai, R. (1987, August). A versatile camera calibration technique for high-accuracy 3D machine vision metrology using off-the-shelf TV cameras and lenses. *IEEE Journal on Robotics and Automation*, *3*(4), 323–344. Retrieved from https://doi.org/10.1109/JRA.1987.1087109 doi:

VanSciver, M., Miller, S., & Hertzberg, J. (2011, February). Particle Image Velocimetry of Human Cough. *Aerosol Science and Technology*, *45*(3), 415–422. Retrieved 2021-05-19, from https://doi.org/10.1080/02786826.2010.542785 doi:

World Health Organization. (n.d.). *Coronavirus overview.* Retrieved from https://www.who.int/health-topics/coronavirus#tab=tab_1 (Accessed: 2021-12-30)

Zhang, R., Li, Y., Zhang, A. L., Wang, Y., & Molina, M. J. (2020, June). Identifying airborne transmission as the dominant route for the spread of COVID-19. *Proceedings of the National Academy of Sciences*, *117*(26), 14857–14863. Retrieved 2021-01-26, from https://doi.org/10.1073/pnas.2009637117 doi:

Zhu, S., Kato, S., & Yang, J.-H. (2006, December). Study on transport characteristics of saliva droplets produced by coughing in a calm indoor environment. *Building and Environment*, *41*(12), 1691-1702. Retrieved from https://doi.org/10.1016/j.buildenv.2005.06.024